

# Zinc-Ion Hybrid Supercapacitors Employing Acetate-Based Water-in-Salt Electrolytes

Jin Han, Alessandro Mariani, Maider Zarrabeitia, Zenonas Jusys, R. Jürgen Behm, Alberto Varzi,\* and Stefano Passerini\*

Halide-free, water-in-salt electrolytes (WiSEs) composed of potassium acetate (KAc) and zinc acetate (ZnAc<sub>2</sub>) are investigated as electrolytes in zinc-ion hybrid supercapacitors (ZHSs). Molecular dynamics simulations demonstrate that water molecules are mostly non-interacting with each other in the highly concentrated WiSEs, while “bulk-like water” regions are present in the dilute electrolyte. Among the various concentrated electrolytes investigated, the 30 m KAc and 1 m ZnAc<sub>2</sub> electrolyte (30K1Zn) grants the best performance in terms of reversibility and stability of Zn plating/stripping while the less concentrated electrolyte cannot suppress corrosion of Zn and hydrogen evolution. The ZHSs utilizing 30K1Zn, in combination with a commercial activated carbon (AC) positive electrode and Zn as the negative electrode, deliver a capacity of 65 mAh g<sup>-1</sup> (based on the AC weight) at a current density of 5 A g<sup>-1</sup>. They also offer an excellent capacity retention over 10 000 cycles and an impressive coulombic efficiency (≈100%).

batteries, possessing a high theoretical capacity (820 mA h g<sup>-1</sup>) and a low electrochemical potential (−0.762 V vs the standard hydrogen electrode).<sup>[4–7]</sup> Nevertheless, it suffers from a low coulombic efficiency (CE) (≈50%) in conventional alkaline electrolytes (e.g., 6 m KOH), caused by the formation of by-products such as zinc hydroxides or zincates.<sup>[3]</sup> Zinc dendrite growth is also an issue. Although dendrite formation could be reduced in mild/neutral electrolytes (e.g., 2 m ZnSO<sub>4</sub>), the CE during plating/stripping of Zn is still unsatisfactory (≈70%) and accompanied by formation of side-products<sup>[3]</sup> such as Zn<sub>4</sub>SO<sub>4</sub>(OH)<sub>6</sub>·5H<sub>2</sub>O.<sup>[8]</sup> In this regard, fluorine-containing electrolytes, for example, 3 m Zn(CF<sub>3</sub>SO<sub>3</sub>)<sub>2</sub>, can suppress dendrite formation and enable a high Zn plating/stripping CE (≈100%).<sup>[9]</sup>

These electrolytes, however, have higher costs compared to aqueous solutions based on fluorine-free salts.<sup>[9]</sup>

A further strategy to improve the reversibility of Zn metal negative electrodes (anodes) is to implement highly concentrated electrolytic solutions, the so-called water-in-salt electrolytes (WiSEs). These electrolytes not only possess a larger electrochemical stability window (ESW) compared to diluted solutions, but also enable an enhanced reversibility of the Zn anode because of the limited amount of free water molecules.<sup>[10,11]</sup> For example, 30 m ZnCl<sub>2</sub>,<sup>[12]</sup> 1 m Zn(TFSI)<sub>2</sub> + 20 m LiTFSI,<sup>[3]</sup> and the concentrated urea/Li(TFSI)<sub>2</sub>/Zn(TFSI)<sub>2</sub><sup>[13]</sup> mixture resulted in an outstanding plating/stripping performance of Zn anodes, offering high CEs (95.4%, 99.9%, and 96.0%, respectively). However, as previously mentioned, these halide-containing salts are quite costly and can be environmentally harmful. Beyond that, LiMn<sub>2</sub>O<sub>4</sub>/Zn and Ca<sub>0.20</sub>V<sub>2</sub>O<sub>5</sub>·0.80H<sub>2</sub>O/Zn cells employing the above mentioned electrolytes demonstrated a limited rate capability and cycling stability,<sup>[13,14]</sup> mostly caused by the cathode materials.

Recently, high concentration acetate-based solutions have emerged as low-cost and halide-free WiSEs,<sup>[15–20]</sup> which inspired us to develop a Zn-containing acetate WiSE. In particular, to address the unsatisfactory rate capability and cycling stability of the Zn cells mentioned above, zinc-ion hybrid supercapacitors (ZHSs),<sup>[21–28]</sup> utilizing an acetate-based WiSE and an activated carbon (AC) as the positive electrode and zinc foil as the negative electrode, respectively, are concerned here.

## 1. Introduction

Since 1799, when Alessandro Volta first invented the voltaic pile, numerous battery systems based on Zn have been developed, including, most recently, rechargeable zinc-ion batteries.<sup>[1–3]</sup> In fact, zinc is an ideal anode material for aqueous

J. Han, A. Mariani, M. Zarrabeitia, R. J. Behm, A. Varzi, S. Passerini  
Helmholtz Institute Ulm (HIU)  
Helmholtzstrasse 11, D-89081 Ulm, Germany

J. Han, A. Mariani, M. Zarrabeitia, A. Varzi, S. Passerini  
Karlsruhe Institute of Technology (KIT)  
P.O. Box 3640, D-76021 Karlsruhe, Germany  
E-mail: alberto.varzi@kit.edu; stefano.passerini@kit.edu

Z. Jusys, R. J. Behm  
Institute of Surface Chemistry and Catalysis  
Ulm University  
Albert-Einstein-Allee 47, D-89081 Ulm, Germany

Z. Jusys, R. J. Behm  
Institute of Theoretical Chemistry  
Ulm University  
Albert-Einstein-Allee 11, D-89081 Ulm, Germany

 The ORCID identification number(s) for the author(s) of this article can be found under <https://doi.org/10.1002/smll.202201563>.

© 2022 The Authors. Small published by Wiley-VCH GmbH. This is an open access article under the terms of the Creative Commons Attribution License, which permits use, distribution and reproduction in any medium, provided the original work is properly cited.

DOI: 10.1002/smll.202201563

First, molecular dynamics (MD) simulations are employed to investigate the interactions among cations, anions, and water molecules. Then the influence of the electrolyte composition on the Zn plating/stripping behavior is studied by varying the ratio of potassium acetate (KAc) and zinc acetate ( $\text{ZnAc}_2$ ). 1 m KAc-1 m  $\text{ZnAc}_2$  (1K1Zn), 10 m KAc-1 m  $\text{ZnAc}_2$  (10K1Zn), 20 m KAc-1 m  $\text{ZnAc}_2$  (20K1Zn), and 30 m KAc-1 m  $\text{ZnAc}_2$  (30K1Zn) are the selected electrolyte compositions. A detailed electrochemical characterization of the Zn plating/stripping process is performed and the best performing electrolyte was selected for the full ZHS. Additionally, post-mortem analysis is carried out by means of SEM and X-ray photoelectron spectroscopy (XPS) to understand the influence of the electrolyte composition on the morphology and chemical composition of the Zn anode surface. Finally, ZHSs featuring AC positive electrodes (cathodes), Zn metal negative electrodes (anodes), and the concentrated 30K1Zn electrolyte were assembled and characterized. These devices delivered a specific capacity of 65 mAh  $\text{g}^{-1}$  at a current density of 5 A  $\text{g}^{-1}$ , together with a high capacity retention over 10 000 cycles and an impressive CE of  $\approx 100\%$ .

## 2. Results and Discussion

### 2.1. SWAXS Patterns and Molecular Dynamics Simulations

The small-wide angle x-ray scattering (SWAXS) patterns (Figure 1a) of the various electrolytes show three different regions<sup>[29]</sup> in the  $q$ -range 0.2–3.5  $\text{\AA}^{-1}$ . At  $q > 1 \text{ \AA}^{-1}$  (i.e., real distances  $r < 6.28 \text{ \AA}$ ) a broad double-peak is always observed. The peak in this region is identified as the main peak in liquid systems and it originates from the interactions to the nearest neighbors. It comprises the first (and sometimes the second) solvation shell. It appears clear that the characteristic double peak of pure water is progressively distorted, indicating that the native water structure is heavily modified at high salt concentrations. The effect is probably more evident in the  $S(q)$  functions reported in Figure S1, Supporting Information, where the two peak components progressively merge, with the lower- $q$  component gradually shifts toward higher  $q$ -values. This behavior indicates for the increase of short-range interactions, which overcome the weaker long-range interactions, as more KAc is added in the system.

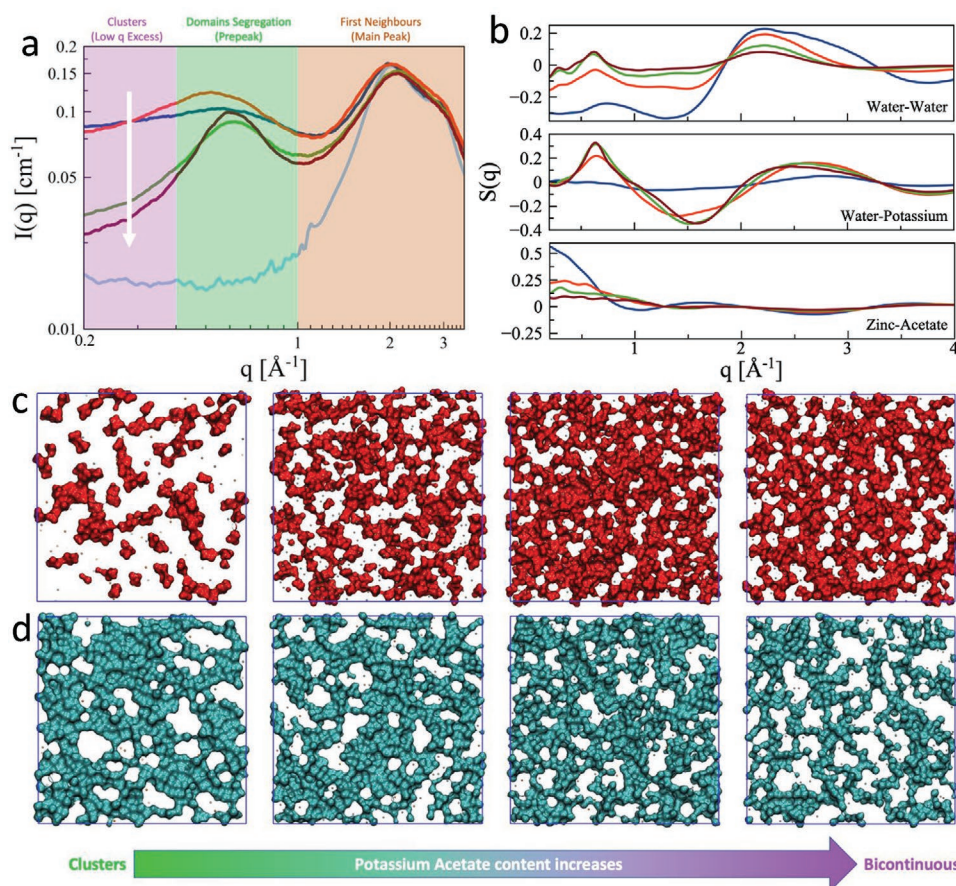


**Figure 1.** a) SWAXS patterns for pure water (cyan), 1K1Zn (blue), 10K1Zn (red), 20K1Zn (green), and 30K1Zn (brown). The white arrow indicates the direction of increasing salt contents. Three different  $q$ -regions are identified and assigned to the corresponding structural correlation, that is, low  $q$  excess ( $q < 0.4 \text{ \AA}^{-1}$ , purple), pre-peak ( $0.4 \text{ \AA}^{-1} < q < 1 \text{ \AA}^{-1}$ , green), and main peak ( $q > 1 \text{ \AA}^{-1}$ , brown). b) Selected partial  $S(q)$ s obtained from the MD simulations for 1K1Zn (blue), 10K1Zn (red), 20K1Zn (green), and 30K1Zn (brown). Snapshots of randomly selected frames of the simulation boxes for c) water molecules in red and d) acetate anions in cyan. Potassium and zinc cations are represented as silver and orange spheres, respectively. Only a 10  $\text{\AA}$  thick slice is shown for clarity, with snapshots for water molecules and acetate anions are complementary. The salts content increases in the direction of the arrow, corresponding to 1K1Zn, 10K1Zn, 20K1Zn, and 30K1Zn.

At  $0.4 \text{ \AA}^{-1} < q < 1 \text{ \AA}^{-1}$  ( $6.28 \text{ \AA} < r < 15.7 \text{ \AA}$ ) we always see an additional feature whose intensity and position depend on the salt content (Table S1, Supporting Information). This peak, often called “pre-peak,” suggests for the presence of mesoscale supra-molecular structures in the order of a nanometer.<sup>[30,31]</sup> Raising the salt concentration makes the pre-peak increasingly sharper, thus hinting to a stricter mesoscopic arrangement at higher KAc content. At  $q < 0.4 \text{ \AA}^{-1}$  a signal is seen for the least concentrated systems, which is associated to pure water (cyan curve in Figure 1a). Such a feature, which decreases for increasing salt contents, is associated to nanoscale objects (in the order of tens of nanometers, if not larger) present in the bulk liquid. Such an uncommon slope is called “Low  $q$  Excess”<sup>[32–36]</sup> (herein after  $LqE$ ). Such complex SWAXS patterns are better analyzed with the help of a model. Thus, some classical MD simulations were performed (Figure 1b) in order to achieve an atomistic-level insight. The comparison between the experimental and theoretical structure functions (Figure S1, Supporting Information) is more than satisfactory, with an almost quantitative agreement for the peaks positions. Regarding the peak intensity, though, while the main peak is always very well reproduced, the pre-peak suffers from systematic over-estimation of its intensity. This is common for highly ionic systems composed of small ions, and the reason is generally ascribed to the lack of polarization effects in standard force fields. It would be possible to achieve better results with polarizable force fields,<sup>[37]</sup> but the computational cost would be excessive for such large systems ( $\approx 20\,000$  molecules per system). Anyhow, for the present scope, the peak position is the main property to be considered, with only some aspects discussed based on relative intensities. Thus the models are perfectly suited. The comparison of the simulation boxes confirms the progressive homogenization of the system, indicating diminished water clusters (Figure 1c) and the decreased size of salt clusters (Figure 1d) as more salt is added.

### 2.1.1. Main Peak and the Water Solvation Shell

Focusing on the  $S_{W-W}(q)$ , that is, water–water interactions, a systematic intensity reduction for the main peak is observed when more salt is added. Furthermore, the high- $q$  component is noticeably more affected than the low- $q$  component of the same peak. Such a dramatic change in the shape of the structure function indicates that the first solvation shell of water is strongly perturbed and disrupted at high salt concentrations, with almost no water molecules as first neighbors. A more insightful visualization of the water solvation shell can be achieved by combining radial distribution functions (RDFs), coordination numbers (CNs), and spatial distribution functions (SDFs), as illustrated in Figure 2, respectively.

Regarding the water–water interaction (panels a and a' in Figure 2), progressive depletion of the first hydration shell is observed, witnessed by the decrease of the intensity of the first sharp peak at  $\approx 2.8 \text{ \AA}$  in the RDFs (panel a). At the same time, a new peak emerges at a larger distance at  $\approx 3.5 \text{ \AA}$ . This correlated change is attributed to indirect “bridged” interactions, where two water molecules interact indirectly via a commonly bonded third species. The average CNs in Figure 2a' show that

the number of water molecules in the first hydration shell decreases by almost a factor of five, passing from 2.92 to 0.63. The SDFs in Figure 2e return visually the hydration state of a central water molecule. Increasing salt content has a clear trend, passing from four direct hydration sites to two sites. At the same time, a new indirect interaction region appears, corresponding to the bridged interaction mentioned before. Together with the partial  $S_{W-W}(q)$ , these observations unambiguously show how at high salt concentrations, the water molecules are mostly non-interacting and thus do not form “bulk-like water” regions. On the other hand, looking at the RDF panels for the interaction of potassium acetate with water (b and d) and the corresponding CN panels (b' and d'), the opposite behavior is seen when comparing with panels a and a'. The interaction gradually becomes stronger, and the water molecules are mainly coordinated to ionic species, with an average of 1.67 acetate anions and 1.81 potassium cations in their first solvation shell. The  $Zn^{2+}$  cations are too few to be statistically relevant, but their decrease around the water molecules upon increasing the salt content occurs. This counter-intuitive behavior will be explained in the following, *vide infra*.

The proposed water solvation state was also experimentally confirmed via Raman spectroscopy. The Raman spectra (Figure S2, Supporting Information) of electrolytes with different concentrations provide insight into the water–acetate interactions. The characteristic  $-\text{OH}$  stretching band at  $\approx 3200 \text{ cm}^{-1}$  can be deconvoluted into five sub-bands, that is,  $\approx 3000$ ,  $\approx 3300$ ,  $\approx 3400$ ,  $\approx 3600$ , and  $\approx 3700 \text{ cm}^{-1}$ , which can be assigned based on the hydrogen-bonding behavior of specific water molecules.<sup>[38]</sup> These sub-bands can be labeled as DAA, DDAA, DA, DDA, and “non-hydrogen-bonding”  $-\text{OH}$  symmetric stretch vibrations, in which D and A are denoted as the donor and the acceptor of a proton, respectively.<sup>[20]</sup> The  $-\text{OH}$  stretch vibrations result from both water–water and water–acetate interactions. The stretching vibrations may be discovered even for 30K1Zn with the highest concentration, as a result that the acetate anion can accept hydrogen bonds from water. In this way, a novel set of similar interactions is established even if the hydrogen bond network of pure water is broken up, thus preserving the Raman band. Meanwhile, the intensity of the DAA peak, derived from the hydrogen bonds accepted by the carboxylic group, gradually increases with increasing concentration, showing that acetate anions progressively coordinate water molecules.<sup>[20]</sup>

### 2.1.2. Pre-Peak and the Acetate Anion Dualism

The second panel of Figure 1b shows the  $S_{W-K}(q)$ , that is, the water–potassium interactions, which contributes most to the pre-peak (see Figure S3, Supporting Information). This means that the mesoscopic heterogeneity mentioned above originates from a characteristic distance between domains mostly composed of water molecules and potassium cations. While the exact morphology and a more in-depth analysis of this specific feature are beyond the scope of this work and will be addressed in a dedicated forthcoming paper, the nature of such mesoscopic organization is briefly discussed. The pre-peak in the SWAXS patterns of liquids made of small molecules (i.e., molecules with a radius of gyration smaller than

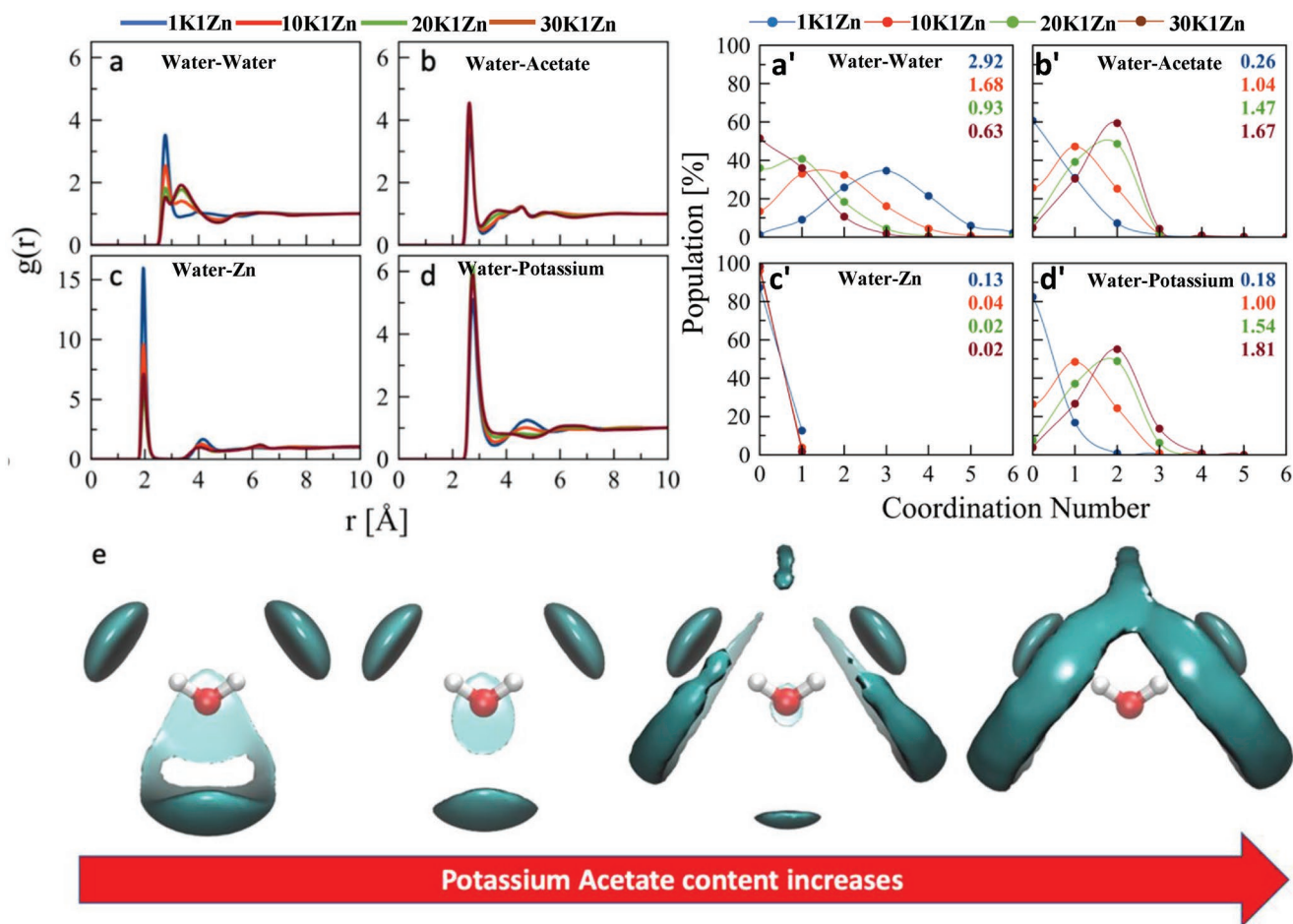


**Figure 2.** a–d) Selected radial distribution functions and a'–d') corresponding coordination numbers.  $O_w-O_w$  (a,a'),  $O_w-O_{Ace}$  (b,b'),  $O_w-Zn$  (c,c'),  $O_w-K$  (d,d'). The numbers in the primed panels are the average coordination numbers. For panels (a–d) and (a'–d'), the color is associated to the salts content as described in the legend. e) Spatial distribution function for the water–water interaction. The clouds are plotted for an iso-value of 1.5 times the average bulk density. The salt content increases in the direction of the arrow, it corresponds to 1K1Zn, 10K1Zn, 20K1Zn, and 30K1Zn, respectively.

1 nm) is not common, with some remarkable exceptions when amphiphilic molecules are concerned.<sup>[39–45]</sup> In those cases, the peak always originates from the formation of a distorted  $L_3$  liquid phase, which is often referred as “sponge-like”<sup>[46]</sup> and which is basically a bicontinuous structure. The formation of this phase is driven by the amphiphilic nature of one (or more) species, which induce a self-segregation by preferentially orienting toward each other compatible molecules or portions of molecules, that is, polar with polar and apolar with apolar. By extracting all relevant partial  $S(q)$ s (Figure 1b), it becomes clear that this case is no exception. In fact, in the  $S_{W-K}(q)$  (Figure 1b) the intense positive contribution, together with the “anti-peaks” (i.e., a peak with a minimum and not a maximum) found in the same  $q$ -region for the acetate–water and acetate–potassium partial  $S(q)$ s (Figure 1b), is the fingerprint of such domains self-segregation, as extensively discussed elsewhere.<sup>[47]</sup> In general, a peak in SWAXS represents structural correlation, while an “anti-peak” appears when there is volume exclusion between the considered species. In our case we have correlation (peak) between water and potassium, and volume exclusion (anti-peak) in the acetate–water and acetate–potassium pairs at that specific distance. This

means that in the region of space where water is in contact with potassium there is no acetate. The presence of slightly hydrophobic and hydrophilic regions in the acetate anion is the main driver for the separation. It is worth noting that pure acetic acid does not show any pre-peak,<sup>[44]</sup> meaning that the driving force of a single methyl group is not enough to generate the distorted  $L_3$  phase. Nevertheless, the additional coulombic interactions introduced by the salification seem to act as a trigger for mesoscopic structuring. The SDFs around the water molecule and the acetate anion are reported in Figures S4,S5, Supporting Information, respectively. They show how the acetate splits the space into two regions, a hydrophilic one interacting with water, the cations, and other carboxylic functional groups, and a hydrophobic one, excluding the polar molecules and only weakly interacting with other methyl groups.

### 2.1.3. Low $q$ Excess and the Zinc Acetate Clusters

The last panel of Figure 1b displays  $S_{Zn-Ace}(q)$ , that is, the zinc–acetate interactions. Here, the only significant feature is

a broad and intense band at the extreme low- $q$  end of the pattern. Based on the discussion above this signal can be assigned to the  $LqE$  visible in the low-salt regime. In fact, the intensity of the scattering of  $S_{Zn-Ace}(q)$  at  $q < 0.4 \text{ \AA}^{-1}$  follows the same trend observed experimentally in the total scattering patterns, that is,  $1K1Zn > 10K1Zn > 20K1Zn > 30K1Zn$ . It is worth noting that the  $LqE$  in the partial  $S_{Zn-Ace}(q)$ s is always visible, but it must be kept in mind that the patterns in Figure 1b are partial  $S(q)$ s, and that the total  $S(q)$  is the sum of all the partial  $S(q)$ s (see Equation (2)). This means that negative contributions in the same region will decrease the overall intensity of the  $LqE$ , potentially even completely deleting that feature by destructive interference. For example, one correlation having an important “anti-peak” in this region is the water–acetate interaction (Figure S3, Supporting Information). The fact that the  $S_{Zn-Ace}(q)$  is the one with the strongest positive contribution to the  $LqE$  means that the nanometric objects responsible for the increased intensity mainly consist of  $ZnAc_2$ , which tends to cluster rather than to homogeneously dissolve in the bulk. Visual inspection of the simulation boxes confirms the increasing homogenization of the system, highlighting the formation of salt clusters that decrease in size as more salt is added (Figure 1d). The fact that the  $LqE$  is diminished at higher salt concentrations suggests that the origin of the increased intensity could be similar to what is observed in some ionic liquid mixtures with various co-solvents. There, when the co-solvent is added in strong excess (ionic liquid mole fraction smaller than 0.2) the ionic liquid tends to aggregate, forming regions of almost pure ionic liquid floating in the co-solvent.<sup>[13]</sup> Such an arrangement is called phase nano-segregation.<sup>[48]</sup> Nevertheless, on a macroscopic scale, the system is homogeneous, liquid, and completely transparent.

## 2.2. Stability of Zn Foil in Variety of Electrolytes

To investigate the stability of Zn in the electrolytes, Zn foils were immersed into 0.5 mL of 1K1Zn, 10K1Zn, 20K1Zn, and 30K1Zn. Photographs were taken when Zn foils were immersed into above solutions for 3 and 7 days, respectively. During the immersion, the zinc foils floated on the surface of the electrolytes as a result of gas formation, except for the one immersed in 30K1Zn. After 3 days, increasing corrosion was observed on the Zn foils immersed in 1K1Zn (Figure 3a), 10K1Zn (Figure 3b), and, especially, 20K1Zn (Figure 3c). Nevertheless, even upon prolonged storage in the 30K1Zn electrolyte (Figure 3d), the Zn foil still maintains its original metallic luster, accompanied only by the precipitation of a crystalline substance. The deposits could be related to the precipitation of the salts (KAc or  $ZnAc_2$ ) from the highly concentrated 30K1Zn as a result of solvent ( $H_2O$ ) evaporation. X-ray diffraction (XRD) patterns (Figure 3e) of the zinc foils immersed for 7 days in the electrolytes were collected to identify the solid products formed on their surface. The characteristic peaks of Zn metal (PDF#04-0831) are still present in the diffractograms of the foils immersed in 1K1Zn and 30K1Zn, while they totally disappear after immersion in 10K1Zn and 20K1Zn. This is consistent with the extensive corrosion of Zn after 7 days. Additionally, ZnO (PDF#21-1486) was also found in the

foils immersed in 1K1Zn and 10K1Zn, further confirming the corrosion of Zn in these diluted solutions. For instance, the Zn foil immersed in 20K1Zn was almost totally dissolved in the electrolyte (see Figure 3c') resulting in the formation of  $Zn_5(CO_3)_2(OH)_6$  (PDF#19-1458),  $Zn(OH)_2$  (PDF#38-0356), and  $C_2H_6O_6Zn_4$  (PDF#19-1472). Nevertheless, the corrosion of Zn is apparently suppressed by the absence of free water molecules in 30K1Zn. Meanwhile, the solute's crystallization in 30K1Zn occurs because the water evaporation makes the electrolyte over-saturated. In addition, the Zn/K molar ratio in the 30K1Zn before and after 7 days of Zn foil immersion has been determined by inductively coupled plasma optical emission spectrometry (ICP-OES). The results (Table S2, Supporting Information) show that the amount of Zn increases only slightly, indicating the relatively good chemical stability of Zn in 30K1Zn. The reason why Zn is chemically stable in 30K1Zn could be elucidated by the simulation results performed in the Section 2.1, even though the corrosion seems an interfacial characteristic. In fact, ions move between the interface and bulk electrolyte regions upon molecular thermal motion and/or the battery operation. In this regard, the characterization of the electrolyte bulk structure is (yet indirectly) very strongly related to the corrosion process. Not to mention that our finding regarding the  $ZnAc_2$  clusters can be linked to a particularly stable zinc ions coordination, which itself is a critical prerequisite for corrosion to occur (i.e., an unfavorable bulk environment for zinc ions would prevent zinc metal dissolution). The dissolution of such clusters at increased concentration apparently lowers the driving force for zinc dissolution, meaning that there is no more a strong enough chemical potential difference between the zinc in the electrode and the zinc in the electrolyte bulk.

## 2.3. Zn Plating/Stripping Behavior and Hydrogen Evolution

To assess the ESW of the electrolytes, linear sweep voltammetry (LSV) measurements were performed using three-electrode cells (Figure 4a) with a stainless steel (SS) disk as working electrode. Notably, both the anodic and the cathodic stability are enhanced when increasing the acetate concentration, that is, going from 1K1Zn to 30K1Zn, as a result of the decreasing fraction of free water molecules. The reversibility of Zn plating/stripping in 1K1Zn (Figure 4b), 10K1Zn (Figure 4c), 20K1Zn (Figure 4d), and 30K1Zn (Figure 4e) was investigated by cyclic voltammetry (CV) in three-electrode cells, employing a Pt disc (2 mm in diameter) as working electrode. The CV curves in 30K1Zn show a superior reversibility for Zn plating/stripping compared with the lower concentration electrolytes. Notably, the CE of Zn plating/stripping in the 30K1Zn electrolyte increased from 98.2% in the 1<sup>st</sup> cycle to 99.3% in the 50th cycle (Figure S6, Supporting Information). The surface of the Pt electrode was furthermore characterized by optical microscopy after the plating/stripping cycles (see Figure S7, Supporting Information). In 1K1Zn electrolyte, some deposits are clearly seen on top of the Pt electrode, which may reflect the irreversibility of the Zn plating/stripping process. However, only a few dead-Zn particles or side products are observed on the Pt electrode when using

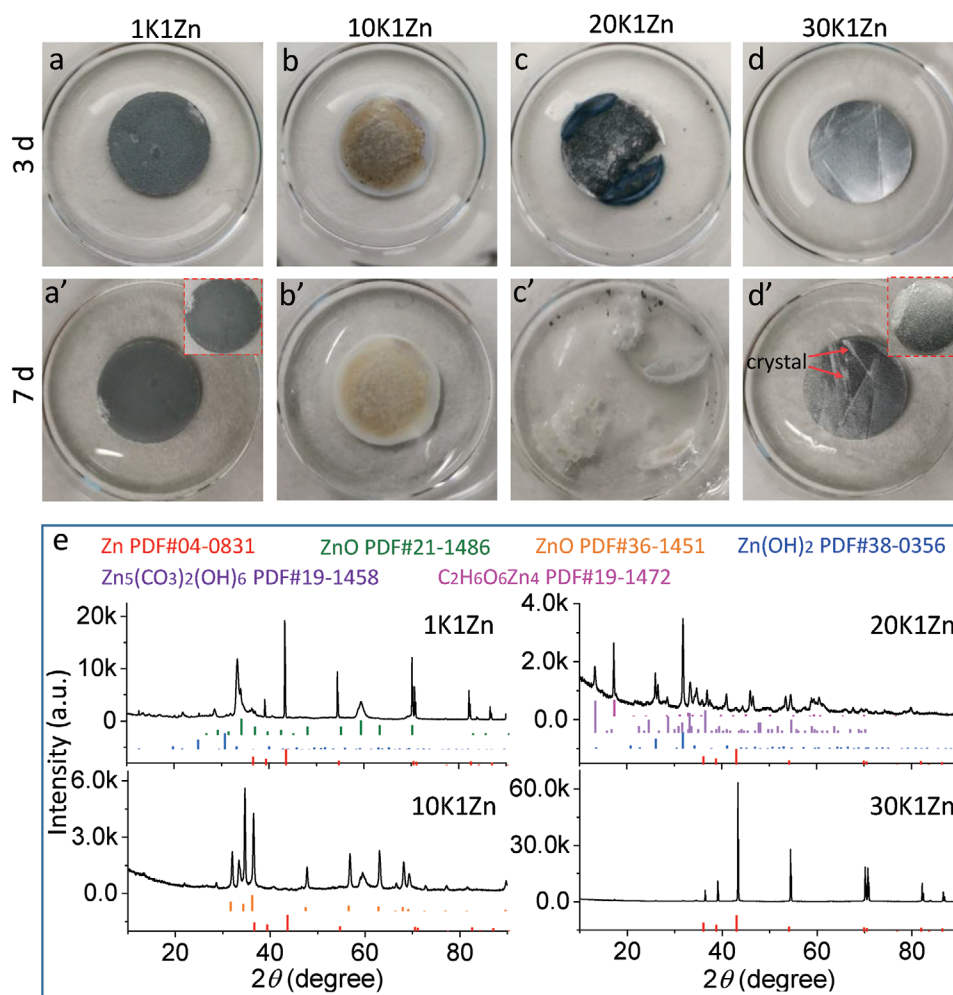


**Figure 3.** Photographs of zinc foils immersed into 0.5 mL of a,a') 1K1Zn, b,b') 10K1Zn, c,c') 20K1Zn, and d,d') 30K1Zn for 3 and 7 days, respectively. e) XRD patterns of the zinc foils (or their remainings) after a 7-day immersion into 1K1Zn, 10K1Zn, 20K1Zn, and 30K1Zn, respectively.

30K1Zn, further confirming the improved reversibility of the process in this electrolyte.

DEMS experiments were performed to investigate the stability of the electrolyte, in particular, hydrogen evolution during Zn plating/stripping.<sup>[49]</sup> A Pt-sputtered fluorinated ethylene-propylene (gas porous) membrane was employed as working electrode. The cell was connected to a mass spectrometer, allowing for selective online detection of gases evolving at the interface between working electrode and electrolyte.<sup>[49,50]</sup> Using this set-up, CVs were recorded (Figure 4f) while performing Zn plating/stripping in 1K1Zn, 10K1Zn, 20K1Zn, and 30K1Zn. The collected mass spectrometric current traces for H<sub>2</sub> ( $m/z = 2$ ) are presented in Figure 4g. The spectra clearly demonstrate hydrogen evolution in the high potential range, which gradually decreased with increasing salt concentrations in the electrolyte. It is proved that corrosion and hydrogen evolution increase with increasing salt concentrations, but become negligible for 30K1Zn, that is, when free water molecules are practically absent. Based on the afore-mentioned results, 1K1Zn and 30K1Zn are selected for further studies.

#### 2.4. Zn Plating/Stripping in Zn||Zn Symmetrical Cells and the Morphology of Cycled Zn Electrode

Galvanostatic plating/stripping measurements were carried out to further investigate the effect of the electrolyte concentration on the Zn, employing a current density of 0.1 mA cm<sup>-2</sup> (each step lasting for 1 h). Voltage profiles are presented in Figure 5a,d, respectively, for 1K1Zn and 30K1Zn. Irregular voltage profiles are clearly recorded in 1K1Zn electrolyte, probably due to hydrogen evolution. Additionally, a rapid cell short circuit is observed, which presumably results from dendritic Zn deposition. The stability and reversibility of the Zn plating/stripping process is largely improved, up to 1200 h, when using 30K1Zn. Interestingly, although the overpotential in this electrolyte is slightly higher than in 1K1Zn, it decreases upon cycling (e.g., see insets of Figure 5d after 1200 h).

The surface morphology of the Zn electrodes was characterized after 100 plating/stripping cycles. The electrode tested in 1K1Zn shows the formation of dendritic Zn crystals (Figure 5c), agglomerated in large globular porous particles with a diameter of around 10 μm (Figure 5b). In contrast, the Zn foil cycled in

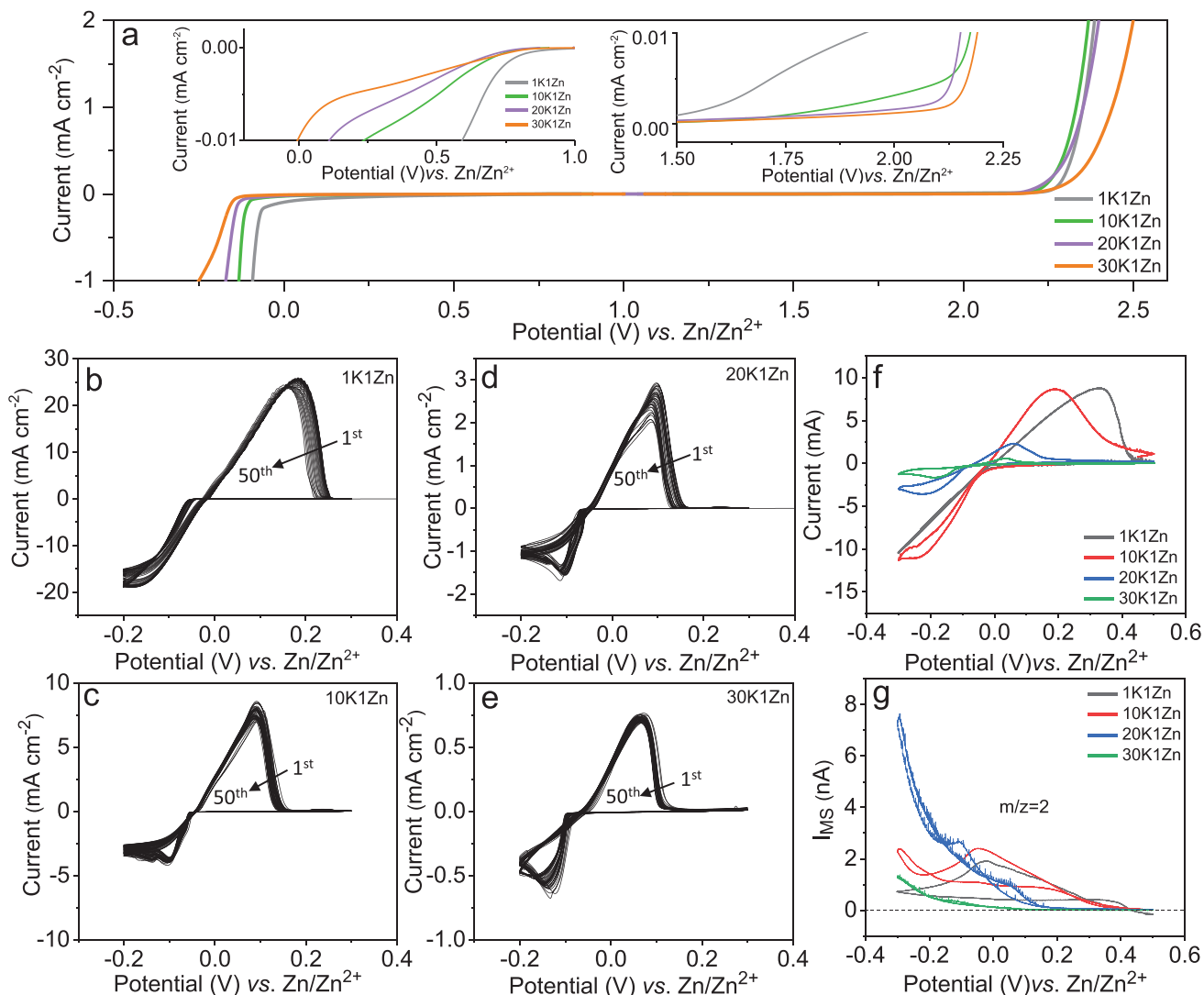


**Figure 4.** a) Electrochemical stability window of 1K1Zn, 10K1Zn, 20K1Zn, and 30K1Zn, employing stainless steel (SS) as working electrode and Zn as both reference and counter electrodes (scan rate 1 mV s<sup>-1</sup>). CVs of Zn plating/stripping in b) 1K1Zn, c) 10K1Zn, d) 20K1Zn, and e) 30K1Zn for the first 50 cycles, performed in a three-electrode glass cell using a Pt disc (2 mm in diameter) as working electrode and Zn as reference and counter electrodes (scan rate 1 mV s<sup>-1</sup>) in the potential range -0.2 to 0.3 V (vs Zn/Zn<sup>2+</sup>). f) CV of Zn plating/stripping in the above mentioned four different electrolytes, employing a commercial Pt electrode (diameter: 2 mm) as working electrode, and Zn as reference and counter electrodes (scan rate 1 mV s<sup>-1</sup>) and g) corresponding selected ion ( $m/z = 2$  for H<sub>2</sub>) currents acquired in potentiodynamic DEMS measurements (scan rate: 0.2 mV s<sup>-1</sup>) in the potential range -0.3 to +0.5 V (vs Zn/Zn<sup>2+</sup>), respectively.

30K1Zn shows a rather smooth surface (see Figure 5e). This is covered by sub-micrometric particles that can only be distinguished at high magnification (see Figure 5f). In combination, these results demonstrate that both hydrogen evolution and dendrite growth are effectively suppressed in the highly concentrated 30K1Zn electrolyte.

## 2.5. Electrochemical Characterization of ZHSs

To further inspect the high reversibility and cycling stability of Zn electrodes in the sustainable and low-cost acetate-based electrolytes, ZHSs including AC as the positive electrode and Zinc as the negative electrode were assembled into coin cells

and characterized. The charge–discharge voltage profiles of the ZHS with 1K1Zn (Figure 6a) demonstrate a plateau in both the low and high working potential range as well as a large, irreversible capacity (108 mAhg<sup>-1</sup>) in the first cycle, where the latter indicates a drastic decomposition of the electrolyte. In addition, a rapid capacity fading occurs within a few cycles of ZHSs with 1K1Zn (see Figure S8, Supporting Information) due to evident electrolyte decomposition during the discharge process, probably resulting from hydrogen evolution taking place at the AC positive electrode when approaching 0 V versus Zn. On the other hand, we only find a very limited irreversible capacity (13 mAhg<sup>-1</sup>) in the first cycle of the ZHS cell with the 30K1Zn electrolyte (Figure 6b). The charge–discharge voltage profiles of the ZHS cell with 30K1Zn at different current densities,

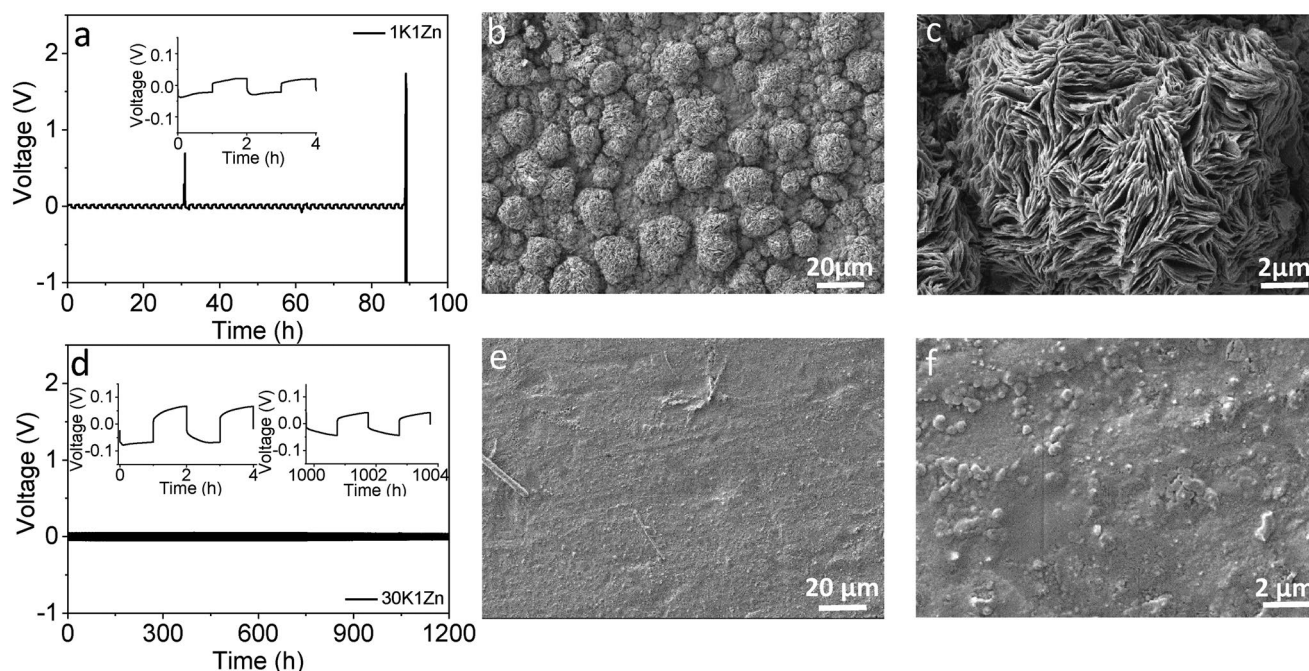


**Figure 5.** Voltage profiles recorded in a Zn||Zn symmetrical cell at  $0.1 \text{ mA cm}^{-2}$  (each half cycle lasting for 1 h, i.e.,  $0.1 \text{ mAh cm}^{-2}$ ) in a) 1K1Zn and d) 30K1Zn. SEM images of the Zn electrodes after 100 plating/stripping cycles in b,c) 1K1Zn and e,f) 30K1Zn

ranging from 1 to  $10 \text{ A g}^{-1}$ , do not reveal any evidence for hydrogen or oxygen evolution (Figure S9, Supporting Information). The cycling performance of the ZHS cell with 30K1Zn was further characterized for a current density of  $5 \text{ A g}^{-1}$  (see Figure 6c,e). A slight capacity increase is noticed in the first few cycles resulting from a decreasing cell polarization as already observed in the plating/stripping tests of symmetric Zn cells (see Figure 5d and related text). On the long term, the delivered capacity remains very stable upon 10000 cycles with the CE approaching 100%. It should be noted that  $\text{MnO}_2$  has been also reported as cathode material of ZHS.<sup>[51]</sup> While such system offers higher capacity than the one proposed in this work, our results are largely superior in terms of capacity retention upon cycling.

After the long-term cycling measurement, the thickness of the cycled coin cells was measured for both electrolytes, 1K1Zn and 30K1Zn, and compared to those of the pristine cells (Figure S10, Supporting Information). The cell with 1K1Zn reached a thickness of  $6.02 \pm 0.01 \text{ mm}$ , almost twice as much as the pristine state ( $3.35 \pm 0.01 \text{ mm}$ ), indicating a notable expansion, most likely due to gas evolution. In contrast, the thickness of the cell featuring 30K1Zn increases only slightly, from  $3.34 \pm 0.01$  to  $3.46 \pm 0.01 \text{ mm}$  after 10000 cycles. This result fits perfectly with the DEMS observation of a suppressed  $\text{H}_2$  evolution and the formation of a rather dense Zn deposit in 30K1Zn (see Figure 5e,f). SEM images of AC electrodes are presented in Figure S11, Supporting Information, pristine electrode, and in Figure S12, Supporting Information, electrodes cycled in 1K1Zn and 30K1Zn. Obvious cracks are seen on the surface of the AC electrode after cycling in 1K1Zn. On the other hand, the surface of the electrode cycled in 30K1Zn seems to be rather uniform, most likely covered by a passivation layer. The cracks on the AC electrode tested in 1K1Zn could be caused by the high

gas pressure indicated by the coin cell expansion. To examine possible side-product formation and the build-up of a passivation layer on the Zn electrodes after long-term cycling in both electrolytes, XRD experiments were carried out (see Figure 6d) both on the pristine and on the cycled electrodes. The XRD pattern of the Zn electrode cycled in 1K1Zn reveals the formation of  $\text{Zn}_5(\text{OH})_6(\text{CO}_3)_2$  (JCPDS:72-1100). However, the pattern of the electrode cycled in 30K1Zn is dominated by the characteristic reflections of metallic Zn (JCPDS: 01-087-0713), with only very minor peaks assignable to Zn(II)O (JCPDS: 80-0075). This indicates that side reactions at the Zn electrode surface are very limited upon cycling in 30K1Zn.

## 2.6. XPS Characterization of Zn Anodes

Additionally, XPS measurements were carried out to confirm the results obtained by XRD and to better understand the chemical composition of the Zn surface. Figure 7 shows Zn 2p, O 1s, and K 2p + C 1s spectra of the two electrodes studied after cycling. The Zn 2p spectra of Zn electrodes cycled in 1K1Zn and 30K1Zn, respectively, can be deconvoluted into two peaks, with binding energies for the Zn  $2p_{3/2}$  peak of around 1024.1 and 1022.0 eV, and 1022.3 and 1021.5 eV for 1K1Zn and 30K1Zn, respectively. Because of the small chemical shifts in the Zn 2p signals, the Zn Auger parameters (the sum of Zn  $2p_{3/2}$  binding energy and Zn  $L_3M_{45}M_{45}$  kinetic energy) were additionally calculated, which are illustrated in Figure 7. This allows to identify different species with even small differences in their Zn 2p binding energy.<sup>[52]</sup> The two peaks observed on the Zn foil cycled in 1K1Zn can be assigned to ZnO (peak at 1022.0 eV, Auger parameter  $2010.1 \pm 0.2 \text{ eV}$ ) and one or more species that will be identified below in the second peak (at 1024.1 eV, Auger

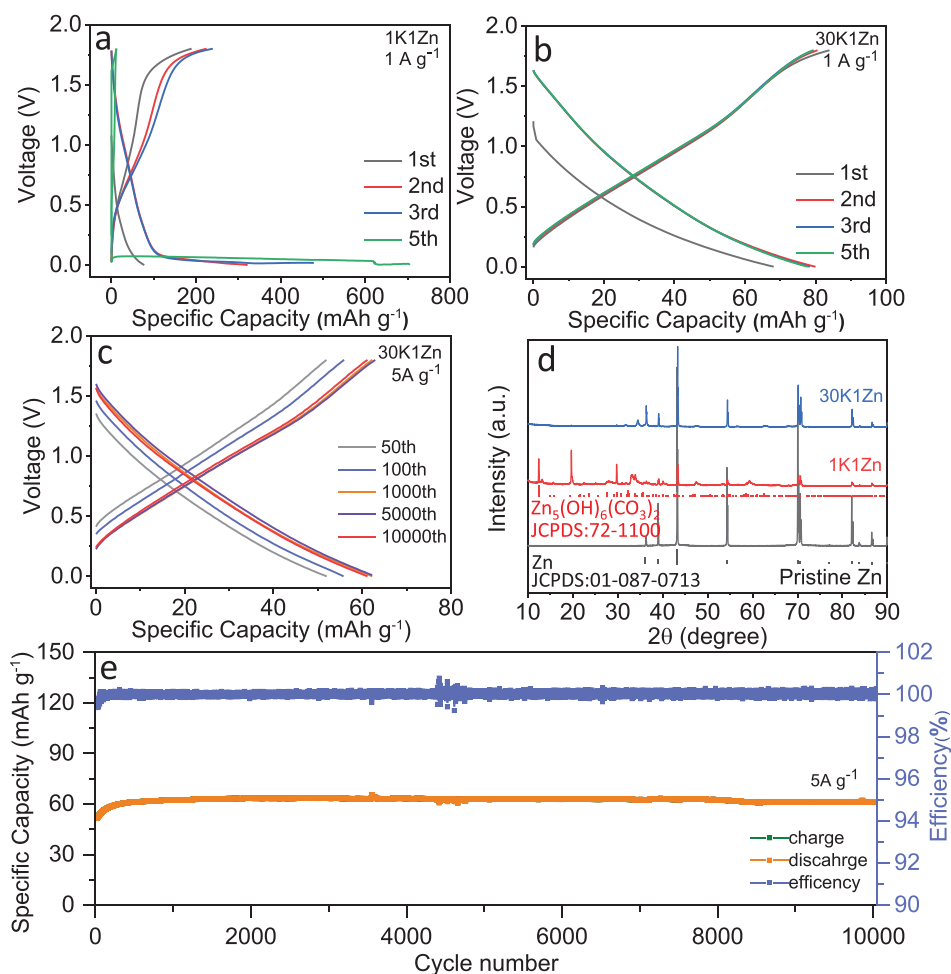


**Figure 6.** Galvanostatic charge–discharge curves recorded at Zn||AC coin cells with a) 1K1Zn and b) 30K1Zn in the voltage range 0–1.8 V at 1 A g<sup>-1</sup>. c) Selected voltage profiles and e) specific capacity and CE recorded upon galvanostatic charge–discharge cycling of a Zn||AC cell at 5 A g<sup>-1</sup> in 30K1Zn. d) XRD patterns of a pristine Zn electrode and Zn electrodes after long-term cycling in 1K1Zn and 30K1Zn.

parameter  $2009.8 \pm 0.2$  eV).<sup>[53]</sup> For the foil cycled in 30K1Zn, the resulting species are ZnO and Zn metal, with Auger parameters of  $2010.5 \pm 0.2$  and  $2013.5 \pm 0.2$  eV, respectively.<sup>[53,54]</sup> This latter finding fully agrees with the results of XRD and SEM imaging, confirming the lower reactivity of 30K1Zn electrolyte during electrochemical cycling. In addition, the O 1s and C 1s spectra of Zn tested in 1K1Zn also confirmed its higher reactivity showing different features (see Figure 7) associated with several oxygen and carbon containing compounds. In particular, as indicated in Figure 7, these features are characteristic of ZnO, Zn(OH)<sub>x</sub>, Zn<sub>x</sub>(CO<sub>3</sub>)<sub>y</sub>, -COH, -COOR (-C=O), and -CH<sub>3</sub>.<sup>[55]</sup> The latter three functional groups are related to the acetate salts,<sup>[20,56]</sup> while the former three reflect Zn-containing species (ZnO, Zn(OH)<sub>x</sub> and Zn<sub>x</sub>(CO<sub>3</sub>)<sub>y</sub>). The peaks observed in O 1s region and as components of the Zn 2p peak at 1024.1 eV (Auger parameter  $2009.8 \pm 0.2$  eV), are consistent with the formation of a ZnCO<sub>3</sub>.<sup>[53]</sup> However, the formation of Zn<sub>5</sub>(OH)<sub>6</sub>(CO<sub>3</sub>)<sub>2</sub> species indicated by the XRD measurements, cannot be confirmed nor excluded<sup>[53]</sup> due to the similar Auger parameter of ZnCO<sub>3</sub> and Zn<sub>5</sub>(OH)<sub>6</sub>(CO<sub>3</sub>)<sub>2</sub>. Besides, the O 1s spectrum recorded on the Zn foil cycled in 1K1Zn exhibits H<sub>2</sub>O traces,<sup>[57]</sup>

while this is not the case for the Zn foil cycled in 30K1Zn. In fact, in the latter case the O 1s signal only shows the presence of -COOR (-C=O) and -COH species from acetate and ZnO, where the latter is also observed in the Zn 2p signal. Finally, the K 2p + C 1s spectrum of 30K1Zn system exhibits the presence of adsorbed potassium ions, probably from potassium acetate, due to the high KAc concentration. Overall, the XPS results clearly confirm the higher reactivity of the 1K1Zn electrolyte compared to 30K1Zn, showing also that the 1K1Zn electrolyte decomposes, forming zinc hydroxides/carbonates. For comparison, the surface of pristine Zn foil, and Zn foil immersed in 30K1Zn for 7 days are analyzed by XPS in Figure S13, Supporting Information. It is found that the pristine Zn foil is covered mainly by ZnO and carbonates due to the passivation of the surface in contact with air. After immersion in 30K1Zn for 7 days, the surface chemistry of Zn is almost unchanged, featuring the same species observed in the pristine sample besides the expected electrolyte traces. This indicates that the Zn foil remains relatively stable when in contact with the concentrated electrolyte. After being cycled in 30K1Zn, the surface species present on the Zn electrode are similar to those detected in the

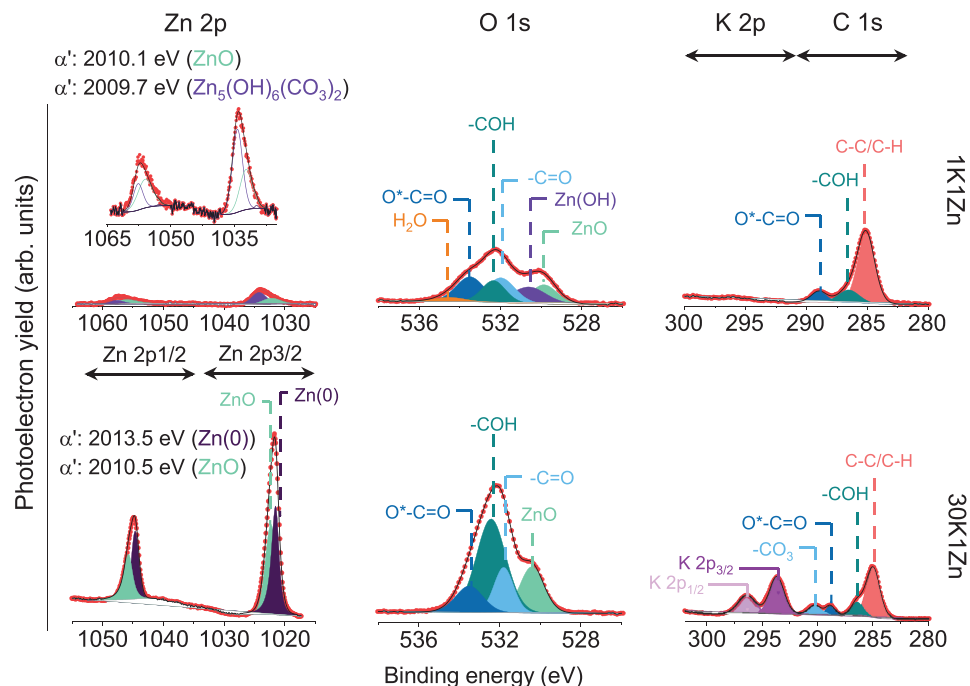


**Figure 7.** Zn 2p, O 1s and K 2p + C 1s photoelectron spectra of the Zn electrodes cycled in (top) 1K1Zn and (bottom) 30K1Zn electrolytes. Zn 2p inset show the calculated Zn Auger parameters.

sample that was simply immersed in the electrolyte. The main differences are the higher electrolyte salts and metallic Zn contribution for cycled Zn in 30K1Zn. The higher concentration of metallic Zn indicates that the reversibly plated Zn is on the surface after the cycling test. These results reveal that the 30k1Zn electrolyte enable stable and reversible Zn electrode operation.

### 3. Conclusion

In conclusion, a series of differently concentrated electrolytes composed of KAc and  $\text{ZnAc}_2$  were developed and characterized. As demonstrated by Raman results, the free water becomes substantially lower with increasing electrolyte concentration. Based on the electrochemical characterization the 30K1Zn electrolyte is the most favorable one for the reversible and stable plating/stripping of Zn, as this concentrated electrolyte could suppress the dendrite growth and  $\text{H}_2$  evolution. ZHSs employing the 30K1Zn electrolyte deliver an extremely good performance (high capacity retention over 10000 cycles and high CE of  $\approx 100\%$ ) compared with the diluted 1K1Zn electrolyte. This is mainly attributed to the highly stable Zn anode operation and the absence of side-product formation, such as, for example,  $\text{Zn}_5(\text{OH})_6(\text{CO}_3)_2$  and  $\text{ZnCO}_3$ , as proven by XRD and XPS.

### 4. Experimental Section

**Materials and Electrolytes:** Zinc foil employed in this experiment were purchased from Goodfellow and had a thickness of 30  $\mu\text{m}$ , the same as in literatures.<sup>[58,59]</sup> Commercial AC (YP50 from Kuraray, specific surface area  $\approx 1000 \text{ m}^2 \text{ g}^{-1}$ ) was kindly supplied by Skeleton Technologies

GmbH. Carbon black (CB) was purchased from Imerys Graphite & Carbon (C-ENERGY Super C45).<sup>[60]</sup> The electrolytes were prepared by dissolving 1, 10, 20, and 30 m potassium acetate (KAc) (Sigma Aldrich,  $\geq 99.0\%$ ) and 1 m  $\text{ZnAc}_2$  (Sigma Aldrich, 99.99%) in 1 kg of Milli-Q  $\text{H}_2\text{O}$ , respectively. They were labeled as 1K1Zn, 10K1Zn, 20K1Zn, and 30K1Zn. To promote the dissolution of salt in water, the solutions were stirred at 40  $^\circ\text{C}$  during dissolution.

**Computational Details:** The MD simulations were carried out using Amber 18 software<sup>[61]</sup> with the GAFF force field.<sup>[62]</sup> Atomic partial charges were obtained with the RESP algorithm from DFT calculations run with Gaussian09e<sup>[63]</sup> at the B3LYP/6-311++G\*\* level of theory. The formal charges for the ionic species were rescaled by a factor of 0.75 to account for polarization and charge-transfer effects, which was validated for highly ionic systems.<sup>[64]</sup> The starting random molecular arrangements were obtained by Packmol<sup>[65]</sup> in boxes with sides of  $\approx 80 \text{ \AA}$ . The number of molecules for each system are listed in Table S3, Supporting Information. The simulation went through different steps, starting from a geometrical relaxation, followed by gradual heating of the system from 0 to 50 K in several NVT (constant number of atoms N, volume V, and temperature T) sessions. The systems were then equilibrated at 300 K for 20 ns in NPT ensemble and further 20 ns in NVT. A final NVT phase of 10 ns was then used for the analysis. For the last phase time steps of 2 fs were used in the SHAKE algorithm,<sup>[66]</sup> and the simulation was saved every 1000 steps, obtaining a final trajectory of 5000 frames with 2 ps in between. Periodic boundary conditions (PBC) along all axes were included to avoid spurious border effects. The temperature was kept constant at 300 K using a Langevin thermostat with a coupling constant of 1  $\text{ps}^{-1}$ . In NPT steps, the pressure was kept constant at 1 atm with a Berendsen barostat. Cutoffs of 8 and 12  $\text{\AA}$  were set for VdW and coulombic interactions, respectively. The Ewald summation method was used to account for the PBC. The simulations reliability was checked by comparing the theoretical and experimental densities (Table S3, Supporting Information). The analyses (structure function calculation, SDFs, and RDFs calculation) were performed exploiting TRAVIS with methodologies described elsewhere.<sup>[67–69]</sup> For each system, three different starting geometries were considered. The results were indistinguishable for each repetition, with deviations in the order of

<0.5% on density values,  $S(q)$  intensities, and RDF intensities. Errors of <0.05% were observed for  $S(q)$  and RDF peaks positions. The total X-ray scattering function,  $S(q)$ , was calculated using the TRAVIS software via:

$$S(q) = \frac{I(q) - \sum_{i \neq j} x_i f_i^2 x_j f_j^2}{\sum_{i \neq j} x_i f_i^2 x_j f_j^2} \quad (1)$$

where  $I(q)$  is the X-ray scattered intensity, and for every  $i, j$  atom pair the respective mole fractions were  $x_i$  and  $x_j$  and the atomic form factors  $f_i$  and  $f_j$ . As clear from Equation (1), it was possible to calculate the partial structure functions by selecting only a subset of the possible  $i$  and  $j$  pairs, with the constraint that the sum of the partial structure functions obtained for all the possible  $i, j$  pairs returned the total structure function  $S(q)$ :

$$S(q) = \sum S_{i,j}(q) \quad (2)$$

Since the partial  $S(q)$ s were not experimentally accessible, they could be extracted only from a model well-representing the real system. The selection of atom pairs was made by setting the mole fraction of the undesired atoms to zero in Equation (2), as implemented in the TRAVIS software.<sup>[7–9]</sup> Practically, this was equivalent to making the undesired atoms transparent to X-rays, thus observing only the scattering pattern caused by the selected atoms in their positions.

**Characterization:** The small and wide angle X-ray scattering patterns were collected using a Xeuss 3.0c (Xenocs – Grenoble, France) equipped with an Eiger2 1M detector (SWAXS) and an Eiger2 500k detector (WAXS). The sample-to-(SWAXS) detector distance was set to 400 mm. A Mo  $K_{\alpha}$  source was employed with a beam size of  $0.7 \times 0.7$  mm<sup>2</sup>, obtaining a flux of  $\approx 10^6$  photons s<sup>-1</sup>. The samples were injected in 1.5 mm o.d. borosilicate capillaries and sealed with solventless hot glue. The sample chamber of the instrument was kept under vacuum ( $p = 50$   $\mu$ bar) during the experiment. Each sample was exposed for 10 min to X-rays to ensure a good signal-to-noise ratio. The empty capillary background was also collected and subtracted from the total scattering curve. A pure water sample was collected and used to scale the intensities in cm<sup>-1</sup>. Data treatment was performed with the Xsact software from Xenocs, PDFgetX3, and some in-house MATLAB code. Raman spectroscopy was carried out at room temperature (20 °C) with a confocal Raman microscope (InVia, RENISHAW) in the spectral range 3800–2800 cm<sup>-1</sup>, using a 532 nm HeNe laser excitation source. The acquisition time was 15 s for each spectrum. The characterization of pristine and cycled Zn electrodes was performed by XRD on a Bruker D8 advance X-ray diffractometer using the Cu  $K_{\alpha}$  radiation (1.5405 Å) in the  $2\theta$  range of 10° to 90° with a step size of 0.01°. Viscosity measurements were carried out using a rheometer (Anton-Paar Physica MCR301) in the cone-plate geometry at 20 °C. The ionic conductivity of the electrolyte was determined in sealed glass conductivity cells (Materials Mates 192/K1) equipped with two platinum electrodes (cell constant of  $(1.0 \pm 0.1)$  cm), using a Bio-Logic conductivity meter at room temperature (20 °C). The pH of electrolytes was measured by a pH meter at room temperature (20 °C). The post-mortem surface chemical composition of cycled Zn in 1K1Zn and 30K1Zn was characterized by XPS, using a monochromatic Al  $K_{\alpha}$  source ( $h\nu = 1487$  eV, 400 W) and a Phoibos 150 XPS spectrometer. High resolution scans were acquired at 20 eV pass energy with 0.1 eV energy steps. The C 1s peak of ubiquitous hydrocarbon, which was set to 285.0 eV, was used as calibration of the binding energy. The evaluation of the Auger parameter was carried out by measuring also the Zn L<sub>3</sub>M<sub>45</sub>M<sub>45</sub> peaks. The CasaXPS software was employed for data fitting using Voigt functions (except for the Zn metal signal, where an asymmetric peak-shape LA(1.4,2,2) was used)<sup>[54]</sup> and a Shirley background. The molar ration of K and Zn in the 30K1Zn before and after 7 days of Zn foil immersion was determined by ICP-OES analysis, carried out on a Spectro Arcos spectrometer (Spectro Analytical Instruments).

**Electrochemical Measurements:** CV of Zn plating/stripping was carried out in a three-electrode cell, using a Pt disc (2 mm in diameter) as working electrode and Zn as reference and counter electrodes and recording 50 cycles at a scan rate of 1 mV s<sup>-1</sup>. The stability of

Zn plating/stripping was evaluated in Zn||Zn symmetrical cells by galvanostatic tests at a current density of 0.1 mA cm<sup>-2</sup> (each half cycle lasted for 1 h). LSVs were performed in a glass cell comprising SS foil (Ni61/Cr22/Mo9/Fe5, thickness:0.2 mm, from Goodfellow) as working electrode and Zn as reference and counter electrode at a scan rate of 1 mV s<sup>-1</sup>. Galvanostatic charge–discharge tests, rate performance, and long-term cycling tests were performed in coin cells composed of commercial AC coated on SS as working electrode and Zinc as counter electrodes. The working and counter electrode were separated by glass microfiber separator (Grade GF/A) discs with a diameter of 16 mm. AC electrodes were prepared by doctor-blade casting slurries with 80 wt% commercial AC, 10 wt% CB (Super C65, IMERYS Graphite & Carbon), and 10 wt% polyvinylidene fluoride (Solef 6020, Arkema Group) on an SS foil as current collector. *N*-Methyl-2-pyrrolidone (anhydrous, Sigma Aldrich) was used as solvent for the slurries. After drying at room temperature, electrodes with a diameter of 12 mm were obtained by punching. These were then further dried at 120 °C under high vacuum. The average active material mass loading was  $\approx 1.5$  mg cm<sup>-2</sup>. LSV and CV tests were conducted with a multichannel potentiostat/galvanostat (VMP3, Biologic Science Instruments, France). A Maccor 4000 Battery system (Maccor, USA) was used for the galvanostatic charge/discharge test at various C-rates at 20 °C.

## Supporting Information

Supporting Information is available from the Wiley Online Library or from the author.

## Acknowledgements

J.H. gratefully acknowledge financial support from the Chinese Scholarship Council. All authors from HIU acknowledge the financial support from the Helmholtz Association. The work of Z.J. was supported by the Federal Ministry of Education and Research (project FKZ 03XP0257C).

Open access funding enabled and organized by Projekt DEAL.

## Conflict of Interest

The authors declare no conflict of interest.

## Author Contributions

J.H. designed and performed the experiment, and prepared the manuscript. A.M. performed the MD simulation, SWAXS measurement and wrote about this part. M.Z. performed and analyzed XPS. Z.J. and R.J.B. performed and analyzed the DEMS measurements. A.V. conceptualized the activities, supervised the experimental work and the revision of the manuscript. S.P. conceptualized and coordinated the activities, provided funding for the work, and revised the manuscript.

## Data Availability Statement

The data that support the findings of this study are available on request from the corresponding author. The data are not publicly available due to privacy or ethical restrictions.

## Keywords

acetate, anode, hybrid supercapacitors, water-in-salt electrolytes, zinc

Received: March 11, 2022

Revised: May 23, 2022

Published online:

- [1] D. Kundu, B. D. Adams, V. Duffort, S. H. Vajargah, L. F. Nazar, *Nat. Energy* **2016**, *1*, 16119.
- [2] H. Pan, Y. Shao, P. Yan, Y. Cheng, K. S. Han, Z. Nie, C. Wang, J. Yang, X. Li, P. Bhattacharya, K. T. Mueller, J. Liu, *Nat. Energy* **2016**, *1*, 16039.
- [3] F. Wang, O. Borodin, T. Gao, X. Fan, W. Sun, F. Han, A. Faraone, J. A. Dura, K. Xu, C. Wang, *Nat. Mater.* **2018**, *17*, 543.
- [4] C. Xu, B. Li, H. Du, F. Kang, *Angew. Chem., Int. Ed. Engl.* **2012**, *51*, 933.
- [5] G. Fang, J. Zhou, A. Pan, S. Liang, *ACS Energy Lett.* **2018**, *3*, 2480.
- [6] H. Li, L. Ma, C. Han, Z. Wang, Z. Liu, Z. Tang, C. Zhi, *Nano Energy* **2019**, *62*, 550.
- [7] J. Ming, J. Guo, C. Xia, W. Wang, H. N. Alshareef, *Mater. Sci. Eng., R* **2019**, *135*, 58.
- [8] L. Dong, X. Ma, Y. Li, L. Zhao, W. Liu, J. Cheng, C. Xu, B. Li, Q.-H. Yang, F. Kang, *Energy Storage Mater.* **2018**, *13*, 96.
- [9] N. Zhang, F. Cheng, Y. Liu, Q. Zhao, K. Lei, C. Chen, X. Liu, J. Chen, *J. Am. Chem. Soc.* **2016**, *138*, 12894.
- [10] L. Suo, O. Borodin, T. Gao, M. Olguin, J. Ho, X. Fan, C. Luo, C. Wang, K. Xu, *Science* **2015**, *350*, 938.
- [11] S. Chen, R. Lan, J. Humphreys, S. Tao, *Energy Storage Mater.* **2020**, *28*, 205.
- [12] C. Zhang, J. Holoubek, X. Wu, A. Daniyar, L. Zhu, C. Chen, D. P. Leonard, I. A. Rodriguez-Perez, J. X. Jiang, C. Fang, X. Ji, *Chem. Commun.* **2018**, *54*, 14097.
- [13] J. Zhao, J. Zhang, W. Yang, B. Chen, Z. Zhao, H. Qiu, S. Dong, X. Zhou, G. Cui, L. Chen, *Nano Energy* **2019**, *57*, 625.
- [14] L. Zhang, I. A. Rodríguez-Pérez, H. Jiang, C. Zhang, D. P. Leonard, Q. Guo, W. Wang, S. Han, L. Wang, X. Ji, *Adv. Funct. Mater.* **2019**, *29*, 1902653.
- [15] Z. Tian, W. Deng, X. Wang, C. Liu, C. Li, J. Chen, M. Xue, R. Li, F. Pan, *Funct. Mater. Lett.* **2017**, *10*, 1750081.
- [16] D. P. Leonard, Z. Wei, G. Chen, F. Du, X. Ji, *ACS Energy Lett.* **2018**, *3*, 373.
- [17] M. R. Lukatskaya, J. I. Feldblyum, D. G. Mackanic, F. Lissel, D. L. Michels, Y. Cui, Z. Bao, *Energy Environ. Sci.* **2018**, *11*, 2876.
- [18] J. Guo, Y. Ma, K. Zhao, Y. Wang, B. Yang, J. Cui, X. Yan, *ChemElectroChem* **2019**, *6*, 5433.
- [19] J. Han, H. Zhang, A. Varzi, S. Passerini, *ChemSusChem* **2018**, *11*, 3704.
- [20] J. Han, A. Mariani, H. Zhang, M. Zarrabeitia, X. Gao, D. V. Carvalho, A. Varzi, S. Passerini, *Energy Storage Mater.* **2020**, *30*, 196.
- [21] H. Wang, M. Wang, Y. Tang, *Energy Storage Mater.* **2018**, *13*, 1.
- [22] S. Chen, L. Ma, K. Zhang, M. Kamruzzaman, C. Zhi, J. A. Zapien, *J. Mater. Chem. A* **2019**, *7*, 7784.
- [23] X. Ma, J. Cheng, L. Dong, W. Liu, J. Mou, L. Zhao, J. Wang, D. Ren, J. Wu, C. Xu, F. Kang, *Energy Storage Mater.* **2019**, *20*, 335.
- [24] Z. Li, Y. An, S. Dong, C. Chen, L. Wu, Y. Sun, X. Zhang, *Energy Storage Mater.* **2020**, *31*, 252.
- [25] H. Tang, J. Yao, Y. Zhu, *Adv. Energy Mater.* **2021**, *11*, 2003994.
- [26] Z. Li, D. Chen, Y. An, C. Chen, L. Wu, Z. Chen, Y. Sun, X. Zhang, *Energy Storage Mater.* **2020**, *28*, 307.
- [27] X. Shi, H. Zhang, S. Zeng, J. Wang, X. Cao, X. Liu, X. Lu, *ACS Mater. Lett.* **2021**, *3*, 1291.
- [28] Y.-G. Lee, G.-H. An, *ACS Appl. Mater. Interfaces* **2020**, *12*, 41342.
- [29] J. C. Araque, J. J. Hettige, C. J. Margulis, *J. Phys. Chem. B* **2015**, *119*, 12727.
- [30] M. Wilson, P. Madden, *Phys. Rev. Lett.* **1994**, *72*, 3033.
- [31] O. Russina, A. Triolo, L. Gontrani, R. Caminiti, *J. Phys. Chem. Lett.* **2012**, *3*, 27.
- [32] A. Mariani, R. Caminiti, F. Ramondo, G. Salvitti, F. Mocci, L. Gontrani, *J. Phys. Chem. Lett.* **2017**, *8*, 3512.
- [33] A. Mariani, R. Dattani, R. Caminiti, L. Gontrani, *J. Phys. Chem. B* **2016**, *120*, 10540.
- [34] M. Campetella, A. Mariani, C. Sadun, B. Wu, E. W. Castner Jr, L. Gontrani, *J. Chem. Phys.* **2018**, *148*, 134507.
- [35] A. Mariani, M. Bonomo, S. Passerini, *Symmetry* **2019**, *11*, 1425.
- [36] O. Russina, A. Sferrazza, R. Caminiti, A. Triolo, *J. Phys. Chem. Lett.* **2014**, *5*, 1738.
- [37] M. Campetella, L. Gontrani, F. Leonelli, L. Bencivenni, R. Caminiti, *ChemPhysChem* **2015**, *16*, 197.
- [38] Q. Sun, *Chin. Phys. Lett.* **2013**, *30*, 126102.
- [39] J. N. Canongia Lopes, A. A. Padua, *J. Phys. Chem. B* **2006**, *110*, 3330.
- [40] M. Tomšič, A. Jamnik, G. Fritz-Popovski, O. Glatzer, L. Vlček, *J. Phys. Chem. B* **2007**, *111*, 1738.
- [41] A. Mariani, P. Ballirano, F. Angiolari, R. Caminiti, L. Gontrani, *ChemPhysChem* **2016**, *17*, 3023.
- [42] I. Pethes, L. Temleitner, M. Tomšič, A. Jamnik, L. Pusztai, *Phys. Status Solidi* **2018**, *255*, 1800127.
- [43] V. T. Liveri, D. Lombardo, M. Pochylski, P. Calandra, *J. Mol. Liq.* **2018**, *263*, 274.
- [44] A. Mariani, A. Innocenti, A. Varzi, S. Passerini, *Phys. Chem. Chem. Phys.* **2021**, *23*, 20282.
- [45] A. Triolo, V. Di Lisio, F. Lo Celso, G. B. Appetecchi, B. Fazio, P. Chater, A. Martinelli, F. Sciubba, O. Russina, *J. Phys. Chem. B* **2021**, *125*, 12500.
- [46] R. Atkin, G. G. Warr, *J. Phys. Chem. B* **2008**, *112*, 4164.
- [47] H. K. Kashyap, J. J. Hettige, H. V. Annapureddy, C. J. Margulis, *Chem. Commun.* **2012**, *48*, 5103.
- [48] A. Mariani, L. Engelbrecht, A. Le Donne, F. Mocci, E. Bodo, S. Passerini, in *Theoretical and Computational Approaches to Predicting Ionic Liquid Properties*, Elsevier, Amsterdam **2021**, pp. 1–67.
- [49] Z. Jusys, M. Binder, J. Schnaidt, R. J. Behm, *Electrochim. Acta* **2019**, *314*, 188.
- [50] B. Qin, A. Schiele, Z. Jusys, A. Mariani, T. Diemant, X. Liu, T. Brezesinski, R. J. Behm, A. Varzi, S. Passerini, *ACS Appl. Mater. Interfaces* **2020**, *12*, 3697.
- [51] Q. Chen, J. Jin, Z. Kou, C. Liao, Z. Liu, L. Zhou, J. Wang, L. Mai, *Small* **2020**, *16*, 2000091.
- [52] C. Wagner, W. Riggs, L. Davis, J. Moulder, G. Muilenberg, *Handbook of X-ray Photoelectron Spectroscopy*, Physical Electronics division, Eden Prairie **1979**, p. 55344.
- [53] L. Dake, D. Baer, J. Zachara, *Surf. Interface Anal.* **1989**, *14*, 71.
- [54] M. C. Biesinger, L. W. Lau, A. R. Gerson, R. S. C. Smart, *Appl. Surf. Sci.* **2010**, *257*, 887.
- [55] R. I. R. Blyth, H. Buqa, F. P. Netzer, M. Ramsey, J. Besenhard, M. Winter, *J. Power Sources* **2001**, *97*, 171.
- [56] J. Han, M. Zarrabeitia, A. Mariani, Z. Jusys, M. Hekmatfar, H. Zhang, D. Geiger, U. Kaiser, R. J. Behm, A. Varzi, *Nano Energy* **2020**, *77*, 105176.
- [57] Y. Xie, P. M. Sherwood, *Chem. Mater.* **1990**, *2*, 293.
- [58] J. Han, A. Mariani, A. Varzi, S. Passerini, *J. Power Sources* **2021**, *485*, 229329.
- [59] J. Han, H. Euchner, M. Kuenzel, S. M. Hosseini, A. Groß, A. Varzi, S. Passerini, *ACS Energy Lett.* **2021**, *6*, 3063.
- [60] P. Ruschhaupt, A. Varzi, S. Passerini, *ChemSusChem* **2020**, *13*, 763.
- [61] D. A. Case, T. E. Cheatham3rd, T. Darden, H. Gohlke, R. Luo, K. M. Merz Jr., A. Onufriev, C. Simmerling, B. Wang, R. J. Woods, *J. Comput. Chem.* **2005**, *26*, 1668.
- [62] J. Wang, R. M. Wolf, J. W. Caldwell, P. A. Kollman, D. A. Case, *J. Comput. Chem.* **2004**, *25*, 1157.
- [63] M. Frisch, G. Trucks, H. Scuseria, et al., *Gaussian09*, Vol. 121, Gaussian, Inc., Wallingford **2009**, p. 150.

- [64] A. Mariani, R. Caminiti, M. Competella, L. Gontrani, *Phys. Chem. Chem. Phys.* **2016**, *18*, 2297.
- [65] L. Martinez, R. Andrade, E. G. Birgin, J. M. Martinez, *J. Comput. Chem.* **2009**, *30*, 2157.
- [66] J.-P. Ryckaert, G. Ciccotti, H. J. Berendsen, *J. Comput. Phys.* **1977**, *23*, 327.
- [67] M. Brehm, B. Kirchner, *J. Chem. Inf. Model.* **2011**, *51*, 2007.
- [68] O. Hollóczki, M. Macchiagodena, H. Weber, M. Thomas, M. Brehm, A. Stark, O. Russina, A. Triolo, B. Kirchner, *ChemPhysChem* **2015**, *16*, 3325.
- [69] M. Brehm, M. Thomas, S. Gehrke, B. Kirchner, *J. Chem. Phys.* **2020**, *152*, 164105.